Super-resolution imaging-based single particle tracking reveals dynamics of nanoparticle internalization by live cells

Article *in* Nanoscale · March 2016

DOI: 10.1039/C6NR01495J

CITATIONS
5

READS
69

3 authors, including:

Yiming Li
Karlsruhe Institute of Technology
4 PUBLICATIONS **27** CITATIONS
SEE PROFILE

Li Shang
Northwestern Polytechnical University
69 PUBLICATIONS **4,040** CITATIONS
SEE PROFILE

Nanoscale

COMMUNICATION

View Article Online
View Journal | View Issue

Cite this: *Nanoscale*, 2016, **8**, 7423

Received 22nd February 2016,
Accepted 14th March 2016

DOI: 10.1039/c6nr01495j

www.rsc.org/nanoscale

Super-resolution imaging-based single particle tracking reveals dynamics of nanoparticle internalization by live cells†

Yiming Li,[a,b] Li Shang[a,b] and G. Ulrich Nienhaus*[a,b,c,d]

By combining super-resolution photoactivation localization microscopy with single particle tracking, we have visualized the endocytic process in the live-cell environment with nanoparticles (NPs) of different size and surface functionalization. This allowed us to analyze the dynamics of NPs interacting with cells with high spatial and temporal resolution. We identified two distinctly different types of pathways by which NPs are internalized *via* clathrin-coated pits (CCPs). Predominantly, NPs first bind to the membrane and, subsequently, CCPs form at this site. However, there are also instances where a NP diffuses on the membrane and utilizes a preformed CCP. Moreover, we have applied this new method to further explore the effects of size and surface functionalization on the NP dynamics on the plasma membrane and the ensuing endocytosis.

NPs hold great promise for diverse applications in energy, biology and medicine;[1–4] their unintended exposure, however, may also pose hazards to human health.[5,6] A detailed understanding of the molecular interactions involved in cellular uptake of NPs is a prerequisite to fully reap the benefits of nanotechnology while avoiding health risks.[7–9] NPs often utilize endocytosis, *i.e.*, the molecular machinery by which cells internalize fluid and material, much in the same way as viruses do. Different endocytosis pathways are known and among these, clathrin-mediated endocytosis (CME), a process utilized by all eukaryotic cells,[10] has been reported to play a prominent role in cellular internalization of many types of NPs.[11–14] In CME, the protein clathrin plays a key role as a component of a coating layer that assembles locally on the inner leaflet of the plasma membrane upon receptor activation. A clathrin-coated pit (CCP) develops by inward budding of the plasma membrane that finally pinches off to form a spherical vesicle inside the cell. Direct visualization of NP uptake requires both high spatial and temporal resolution due to the nanoscale nature of the cellular machinery and the fast molecular dynamics in the living biological environment.[15,16]

Recent advancements in super-resolution fluorescence microscopy have extended the image resolution far beyond the diffraction limit.[17] For example, localization-based super-resolution microscopy such as photoactivation localization microscopy (PALM) routinely yields images resolved to tens of nanometers,[18–20] opening a whole new world of structural detail in biological systems.[21,22] Typically, an individual CME process happens within tens of seconds.[23] It also takes at least seconds to collect data for reconstructing a single PALM image of CCPs, thus making it challenging to track fast CME dynamics. SPT, with its distinct advantage of high temporal resolution, appears as an attractive complementary approach to track NPs with high spatial and temporal resolution while observing cellular responses using super-resolution PALM imaging. Here we demonstrate the first example of combining SPT and PALM to visualize internalization of NPs by living cells (see ESI, Fig. S1 and S2†).

To visualize CCPs in COS-7 cells by using PALM, we transfected the cells with a fusion protein of the clathrin light chain (CLC) and the fluorescent protein mEos2, CLC-mEos2, according to previously established procedures.[24] mEos2 is a variant of mEosFP, a protein which changes its fluorescence emission from green to red upon photoactivation by ~400 nm irradiation,[25] which is essential for PALM imaging. To ensure that the functional integrity of clathrin is not compromised by the added fluorescent protein domain,[26] we co-stained CCPs of a fixed transfected COS-7 cell with an antibody against the clathrin heavy chain. The overlay of immunofluorescence and CLC-mEos2 staining (see ESI, Fig. S3†) clearly reveals that CCPs can be visualized in our transfected cells.

Polystyrene (PS) NPs are widely employed in many applications, *e.g.*, as biosensors,[27,28] in photonics[29,30] and for

[a]*Institute of Applied Physics, Karlsruhe Institute of Technology (KIT), Wolfgang-Gaede-Str. 1, 76131 Karlsruhe, Germany. E-mail: uli@uiuc.edu*
[b]*Institute of Nanotechnology, Karlsruhe Institute of Technology (KIT), Hermann-von-Helmholtz-Platz 1, 76344 Eggenstein-Leopoldshafen, Germany*
[c]*Institute of Toxicology and Genetics, Karlsruhe Institute of Technology (KIT), Hermann-von-Helmholtz-Platz 1, 76344 Eggenstein-Leopoldshafen, Germany*
[d]*Department of Physics, University of Illinois at Urbana-Champaign, Urbana, IL 61801, USA*

†Electronic supplementary information (ESI) available: Experimental section, supporting figures and videos. See DOI: 10.1039/c6nr01495j

self-assembling nanostructures.[31] Therefore, we employed colloidally stable, carboxylate-modified fluorescent PS NPs of different sizes (for physicochemical characterization, see Table 1) to observe their internalization by CLC-mEos2 expressing COS-7 cells. Earlier studies reported that PS NPs with a core size of 40 nm (PS40) are internalized by murine melanoma cells B16-F10 predominantly *via* CME.[32] By using chlorpromazine as an inhibitor known to suppress CME, we observed about 40% decreased fluorescence of internalized PS40 NPs by COS-7 cells (see ESI, Fig. S4†), indicating a significant role of CME in their uptake. To estimate the CCP size and number of NPs bound per CCP, we exposed COS-7 cells for 10, 20, 30 and 40 min to a 1 : 1 mixture of PS40 NPs of two different emission colors prior to fixation (see ESI, Fig. S5 and S6†).[33] Even after 40 min of incubation, the majority of spots were still singly colored; only 20% were from co-localized green and red NPs. This result clearly proves that only a small number of PS 40 NPs congregate within a single CCP. Moreover, regardless of incubation time, the mutual displacement of colocalized green and red NPs yielded ~160 nm for the size of the NP binding cavities, as expected for CCPs.[24]

Compared with conventional TIRF images, the CLC-mEos2 PALM images displayed much better resolved, typically ring-shaped structures (Fig. 1). We investigated the size of CCPs colocalized with and without PS40 NPs in detail. In earlier work, indirect evidence based on fluorescence intensity measurements suggested that the size of CCPs varies with the size of the internalized cargo.[34] Our PALM images allowed us to directly determine the size of the CCPs loaded with PS40 NPs (Fig. 1). The choice of the bin time window is critical for size determination based on PALM images of live cells; here, we took a time bin of 30 s (see ESI, Fig. S7†). As shown in Fig. 1, the mean size of bare CCPs without NPs was 150 ± 2 nm. However, upon incorporating PS40 NPs, CCPs were markedly enlarged to 182 ± 6 nm. This observation thus provides direct quantitative evidence that CCP size increases with cargo loading.

The PALM image of a COS-7 cell (bottom membrane) expressing CLC-mEos2 displays much sharper features than the normal TIRF microscopy image (Fig. 2a). To minimize image blurring due to movement of the CCPs during image acquisition, we reconstructed PALM images from time windows of 15 s, *i.e.*, 500 camera frames of 30 ms exposure time. Additional dynamic information with higher time resolution (30 ms) is provided by NP trajectories obtained in the second color channel (Fig. 2b). In the combined plots of the PALM image and NP trajectories (Fig. 2c), the region marked by the box is shown expanded in Fig. 2d for different time intervals over a total length of 150 s; end points are given in

Table 1 Physico-chemical characterization of bare and transferrin (Tf)-functionalized PS NPs. Dynamic light scattering and ζ-potential measurements were performed in serum-free DMEM using a Zetasizer Nano ZS (Malvern Instruments, Malvern, UK) at 25 °C. Each data point was calculated as an average of 5 runs of 100 individual measurements. Comparison of the diameters of PS40 and PS40-Tf NPs shows that Tf forms multiple layers on the NP surface

Sample	Diameter (nm)	ζ in DMEM (mV)
PS40	62 ± 3	−23.7 ± 1.1
PS40-Tf	101 ± 9	−8.4 ± 0.6
PS40-PEG(10k)-Tf	115 ± 6	−9.5 ± 0.7
PS20	36 ± 1	−33.7 ± 1.9
PS200	216 ± 2	−33.2 ± 2.7

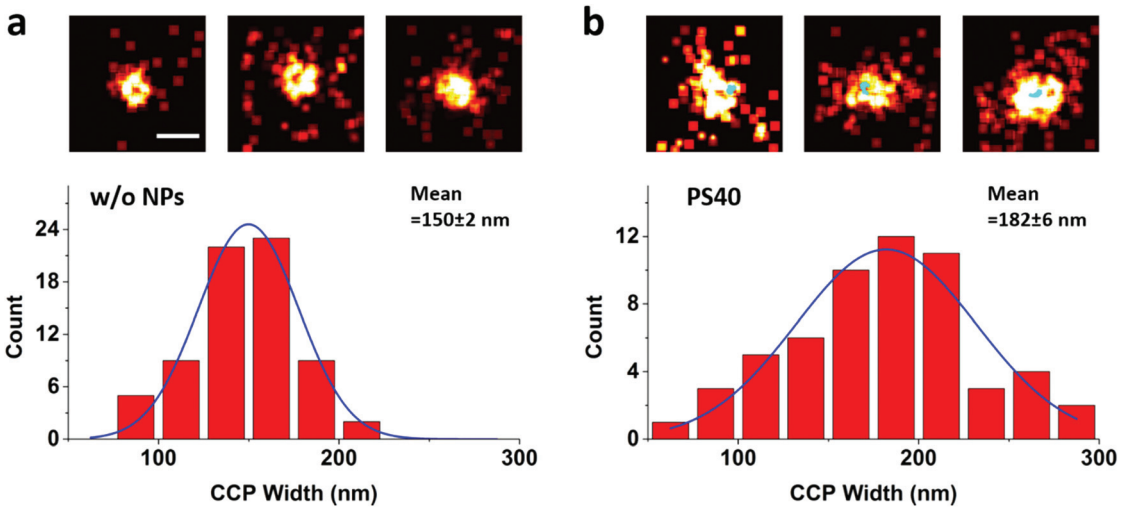

Fig. 1 Typical PALM images of CCPs with and without colocalized PS40 NPs and histograms of measured size distributions. a, PALM images of CCPs without NPs (top) and their size distribution (bottom). b, PALM images of CCPs with colocalized PS40 NPs (top) and their size distribution (bottom). All PALM images were reconstructed from 1000 frames of 30 ms. The trajectories of PS40 NPs during this time interval (in cyan) were overlaid with the PALM images of the CCPs. For each CCP, density profiles along the short axis within a 60 nm wide strip covering the central region were calculated and fitted with a Gaussian to obtain the full-width half maximum (FWHM) as the diameter of an individual CCP. The mean diameters over the entire CCP populations quoted in the figure were extracted from Gaussian fits to the histograms (blue lines). Scale bar, 200 nm.

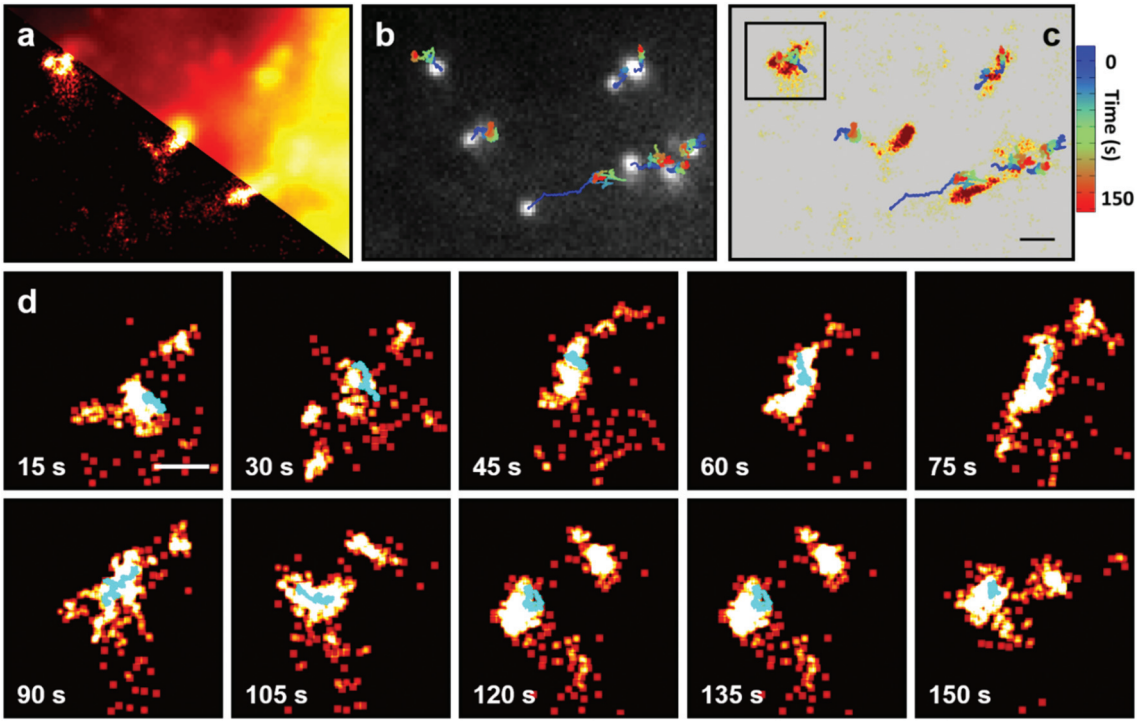

Fig. 2 Visualization of interactions between PS40 NPs and CCPs on COS-7 cells. a, Conventional wide field image (top) and PALM image of CCPs (bottom). b, Trajectories of PS40 NPs diffusing on the plasma membrane of a COS-7 cell. c, Overlap of the PS40 NP trajectories with the PALM image of the CCPs. The time in the trajectories is color-coded, as shown by the bar on the right. d, Ten close-up views of the region indicated by the square in panel c; each image is a 15 s PALM image up to the time indicated in the panel overlaid by the corresponding NP trajectory (in cyan). Scale bars, 1 μm (c) and 500 nm (d).

the individual figures. This image sequence shows a representative time course of an internalization event. From 0–60 s, the particle is confined to a small region, and there is little movement of the CCP in the PALM image. From 60–120 s, the trajectory of the PS40 NP displays directed motion over a short distance during which the CCP structure becomes more extended and closely follows the NP, indicating co-movement of the PS40 NP and the CCP. For the remaining 30 s, both structures again remain confined to a small region. Interpretation of the different phases requires more elaborate analysis presented below.

For quantitative analysis of the NP trajectory, we have applied a rolling-window algorithm to compute the local mean square displacement (MSD) as a function of time (time window 3 s, step size 0.6 s).[35] The MSD was fitted by a power law, MSD = Γt^{α}, with the transport coefficient, Γ, and the time exponent, α, which carries information about the local type of motion: free diffusion ($\alpha = 1$), anomalous subdiffusion ($\alpha < 1$, hindered diffusion) and superdiffusion ($\alpha > 1$, active transport involved).[36,37] We note that the power law expression can formally be recast into the relation for free diffusion, MSD = $4D(t)t$, by introducing a time-dependent diffusion coefficient $D(t) = \frac{1}{4}\Gamma t^{\alpha-1}$. In Fig. S8,† we show two examples of NP trajectories together with their associated local MSD functions, the curvatures of which clearly reveal different types of motion. In Fig. S9,† we compare the time dependence of α for the trajectory shown in Fig. 2d with a simulated one for free diffusion. Even for the simulated trajectory, $\alpha \neq 1$ due to insufficient sampling, but the histogram of α-values peaks around one. For the experimental trajectory, deviations from one are more prevalent in the α-histograms; values near one are suppressed. There are extended phases of hindered diffusion ($\alpha < 1$ for 54% and 50% during the first 60 and the last 30 s of the trajectory) alternating with superdiffusive transport ($\alpha > 1$). Large α-values are predominant (>80%) for the time window 60–120 s, during which the trajectory of the PS40 NP displays directed motion (Fig. 2d). This quantitative analysis lends further support to the notion that the NP is not free to diffuse on the membrane but tightly associated with the CCP and dragged around together with the CCP by the associated internalization machinery. NP movement thus reflects the dynamics of the CCP governed by its interactions with the submembranous cytoskeletal network.

From PALM/SPT data sets of a total of 63 NP–CCP internalization events, we found two distinctly different types of encounters between PS 40 NPs and COS-7 cells (Fig. 3). In more than 90% of the events (58/63, see ESI, Fig. S10† for additional examples), NPs first adhered to the plasma membrane without clathrin being visible (type I encounter, Fig. 3a–d). Then, the CCP signal gradually increased, indicating recruitment of clathrin to this site. In this period of 55 ± 23 s duration ($n = 20$), the emission intensity of NPs stayed essentially constant. After the CCP signal had peaked, the NP intensity began to decrease (Fig. 3c). TIRF excitation is

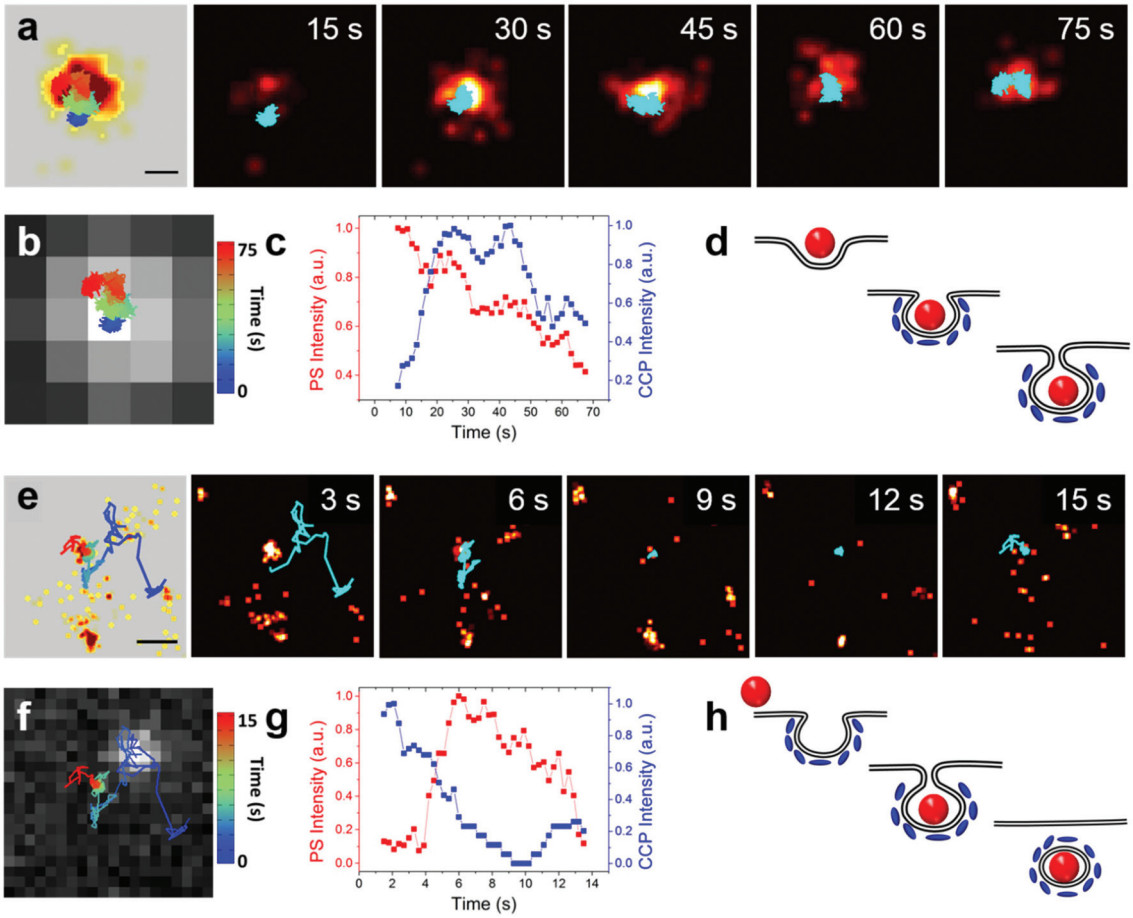

Fig. 3 Visualization of two types of uptake events of PS40 NPs by CCPs. a, Overlay of NP trajectory for 75 s and associated PALM image of the CCP (type I), and five sequential 15 s views of the process. b, NP trajectory on top of raw data, showing a lateral shift of the NP during uptake. c, Time dependence of the (normalized) fluorescence intensity of PS40 NP and CCP during uptake. d, Schematics of the sequential stages during type I endocytosis of PS40 NP. Red: NP, blue: clathrin. e, Overlay of the PS NP trajectory for 15 s and the associated PALM image of the CCP (type II), and five sequential 3 s views of the process. f, PS40 NP trajectory on top of raw data. g, Time dependence of the (normalized) fluorescence intensity of PS40 NP and CCP during uptake. h, Schematics of the sequential stages during type II endocytosis of PS NPs. Red: NP, blue: clathrin. Scale bars, 100 nm (a) and 500 nm (e).

exponentially sensitive to the distance of the fluorescent marker from the surface, so the intensity decrease indicates an axial displacement, as expected for internalization. In the late stage (45–75 s), a 100 nm lateral movement was observed in both the PALM image of the CCP and the NP trajectory (see ESI, movie S1† and Fig. 3b), likely due to the interaction between CCP and submembranous cytoskeleton during internalization of NPs in the intracellular region. We emphasize that thermal drifts of the microscope stage are much smaller, as confirmed by control experiments with PS40 NPs on glass surfaces (see ESI, Fig. S11†). Only a few times (5/63, see ESI, Fig. S12†), we observed that PS40 NPs diffused laterally on the plasma membrane and became trapped in a pre-existing CCP (type II encounter, Fig. 3e–h). Subsequently, the CCP signal continuously decreased, signaling internalization. After ~13 s, both the CCP and PS40 signals disappeared (Fig. 3g), suggesting that the CCP had been completely pinched off the membrane and internalized (Fig. 3h).

We further extended our internalization studies to PS NPs of different sizes and modified surface ligands (Fig. 4). For carboxylated PS NPs with 200 nm diameter (PS200 NPs), not a single cell out of 31 showed a sign of interaction with CCPs (Fig. 4a and f). Apparently, the NPs were simply too big to be internalized *via* this route. Accordingly, the PS200 uptake level did not appreciably change upon treatment of COS-7 cells with chlorpromazine (see ESI, Fig. S4†). For carboxylated PS NPs with 20 nm diameter (PS20 NPs, Fig. 4d) and PS40 NPs (Fig. 4b), we found colocalization with CCPs for more than 50% of the cells, and ~5% of the observed PS NP trajectories colocalized with CCPs (Fig. 4f). This percentage is significantly greater than our expectation for randomly placed particles (0.2%, see ESI, Fig. S13†) but less than the value of 37% that we determined for transferrin (Tf), a protein known to internalize exclusively *via* CME (see ESI, Fig. S14 and S15†). Presumably, activation of CME is less efficient for carboxylated PS NPs than for Tf (Fig. 4f), for which specific receptors reside in the

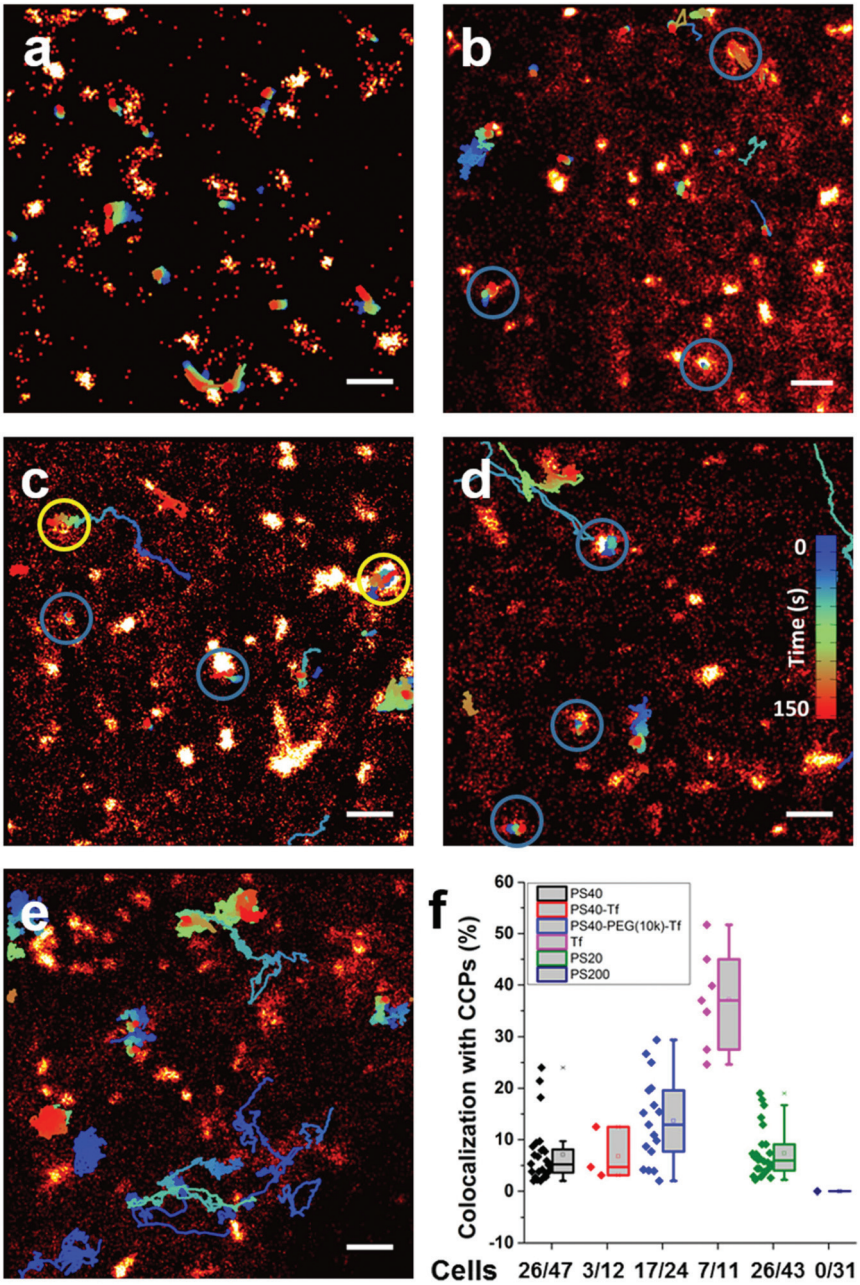

Fig. 4 Comparison of different PS40 NPs interacting with CCPs on COS-7 cells. a, Overlay of PS200 NP trajectories and CCPs. b, Overlay of PS40 NP trajectories and CCPs. c, Overlay of PS40-PEG(10K)-Tf NP trajectories and CCPs. d, Overlay of PS20 NP trajectories and CCPs. e, Overlay of PS40-Tf NP trajectories and CCPs. f, Fraction of different PS NPs colocalized with CCPs; for comparison, data on fluorescently labelled Tf are also included. Blue and yellow circles indicate Type I and Type II events, respectively. Scale bars, 1 μm.

plasma membrane. To examine if Tf conjugation can enhance the interaction, we attached the protein to PS NPs either by direct binding to the NP surface (PS40-Tf) or *via* a 10 kDa PEG linker (PS40-PEG(10k)-Tf), (for synthesis and characterization, see ESI†). For PS40-Tf NPs, only three out of twelve cells showed NPs colocalized with CCPs (Fig. 4e and f) whereas, for PS40-PEG(10k)-Tf NPs, we observed colocalization for 17 out of 24 cells (Fig. 4c and f). The median colocalization fraction (13%) is also markedly higher than for bare PS NPs. These results indicate that Tf tethering to the NP surface enhances binding to CCPs, but only if the Tf protein is attached flexibly enough to enable efficient receptor interactions. Interestingly, a larger fraction of PS40-PEG(10k)-Tf NPs were found to undergo type II internalization (17%, see ESI, Fig. S12†) than bare PS40 NPs (8%) and PS20 NPs (9%).

In order to further understand the effect of surface ligand on NP–CCP interactions, we analyzed PS NP dynamics on the membrane (details see ESI†).[38] Interestingly, very different

dynamics were found for PS40-Tf and PS40-PEG(10k)-Tf NPs on the membrane. For the majority of PS40-Tf NPs (72%, see ESI, Fig. S16†), we observed fast diffusion, similar to what we observed by spinning disk confocal imaging of the top cell surface (see ESI, Fig. S17–19 and Movies S2–4†). These results indicate weak binding of PS40-Tf NPs to the COS-7 cell membrane, which may explain the low uptake yield of PS40-Tf NPs and their small degree of colocalization with CCPs. This is in agreement with earlier work, in which carboxylated NPs with physisorbed rather than covalently bound Tf led to markedly suppressed internalization with respect to bare NPs.[39] Tf enhances internalization only upon specific interaction with its cognate receptor. If, however, the interacting receptor recognition site is not exposed, the resultant interaction is apparently weaker than that of bare carboxylated NPs. Likewise, PS40-PEG(10k)-Tf NPs have a more mobile population (see ESI, Fig. S20†) on the membrane compared to bare PS40 NPs. Their higher average mobility enables them to scan the plasma membrane in search for CCPs, and their tethered Tf then provides the specific interaction required to stay at the site for internalization. In combination, both effects explain the enhanced fraction of type II encounters that we have observed.

In summary, by combining super-resolution imaging with SPT, we have achieved both high spatial and temporal resolution, allowing us to visualize the CME of PS NPs by living cells. We observed two distinctly different types of NP–CCP encounters. In the majority of events, NPs first attached to the membrane, and a CCP subsequently developed at this site. However, we have also encountered events where a NP diffuses on the membrane and utilizes a preformed CCP. This behavior is reminiscent of the cellular entry of the influenza virus, where Zhuang and coworkers reported that most viruses take the CME pathway *via* newly-formed CCPs.[26]

Size and surface ligands of NPs are known to be key determinants affecting endocytosis,[40,41] but the underlying detailed interactions have yet remained elusive. By tracking PS NPs of different sizes and surface functionalities with nanoscale spatial resolution, we found that small PS20 and PS40 NPs were readily internalized *via* CCPs, whereas large PS200 NPs were completely rejected by CME. Moreover, we observed that uptake by CME can be markedly enhanced by tethering Tf *via* a flexible PEG linker to the PS NP surface.

Quantitative analysis of NP diffusion on the membrane yielded further insights into the interactions with the cell membrane. Unlike PS20 NPs, which diffuse swiftly on the plasma membrane, PS40 and PS200 NPs showed tight confinement on the membrane (see ESI, Fig. S16†), presumably due to membrane compartments formed by cortical actin,[42,43] and we observed only very few long-range trajectories. In contrast, both types of Tf-conjugated PS40 NPs showed a fast-diffusing population (see ESI, Fig. S20†) and, especially for PS40-Tf NPs, trajectory analysis revealed a high mobility on the membrane (Fig. 4e). However, we found enhanced uptake only for PS40-PEG(10k)-Tf NPs. Although PS40-Tf NPs quickly scan the membrane, their weaker interaction with plasma membrane receptors apparently prevents their trapping in CCPs. These results indicate that the strength of the interaction between the CCP and the NP, governed by NP surface chemistry, is also important for efficient uptake during the random walk search on the membrane.[16] Finally, we note that, although we have focused here on CME, one can easily adapt our approach to studies of other endocytosis mechanisms, exocytosis and NP–cell interactions in general.

Acknowledgements

This work was funded by the KIT within the context of the Helmholtz Program STN, and by Deutsche Forschungsgemeinschaft (DFG) grants GRK 2039 and Ni291/12-1. Y. L. acknowledges support by a fellowship from the Karlsruhe School of Optics and Photonics (KSOP). L. S. thanks the Carl-Zeiss-Stiftung for a postdoctoral fellowship.

References

1 R. K. Jain and T. Stylianopoulos, *Nat. Rev. Clin. Oncol.*, 2010, **7**, 653–664.
2 M. J. Sailor and J.-H. Park, *Adv. Mater.*, 2012, **24**, 3779–3802.
3 A. B. Djurisic, Y. H. Leung and A. M. Ching Ng, *Mater. Horiz.*, 2014, **1**, 400–410.
4 P. D. Howes, R. Chandrawati and M. M. Stevens, *Science*, 2014, 346.
5 A. Nel, T. Xia, L. Mädler and N. Li, *Science*, 2006, **311**, 622–627.
6 S. Sharifi, S. Behzadi, S. Laurent, M. Laird Forrest, P. Stroeve and M. Mahmoudi, *Chem. Soc. Rev.*, 2012, **41**, 2323–2343.
7 A. E. Nel, L. Mädler, D. Velegol, T. Xia, E. M. V. Hoek, P. Somasundaran, F. Klaessig, V. Castranova and M. Thompson, *Nat. Mater.*, 2009, **8**, 543–557.
8 T.-G. Iversen, T. Skotland and K. Sandvig, *Nano Today*, 2011, **6**, 176–185.
9 L. Treuel, X. Jiang and G. U. Nienhaus, *J. R. Soc., Interface*, 2013, **10**, 20120939.
10 H. T. McMahon and E. Boucrot, *Nat. Rev. Mol. Cell Biol.*, 2011, **12**, 517–533.
11 S. D. Conner and S. L. Schmid, *Nature*, 2003, **422**, 37–44.
12 B. D. Chithrani and W. C. W. Chan, *Nano Lett.*, 2007, **7**, 1542–1550.
13 X. Jiang, C. Röcker, M. Hafner, S. Brandholt, R. M. Dörlich and G. U. Nienhaus, *ACS Nano*, 2010, **4**, 6787–6797.
14 L. Yang, L. Shang and G. U. Nienhaus, *Nanoscale*, 2013, **5**, 1537–1543.
15 E. Sun, J. He and X. Zhuang, *Curr. Opin. Virol.*, 2013, **3**, 34–43.
16 K. Welsher and H. Yang, *Nat. Nanotechnol.*, 2014, **9**, 198–203.
17 S. W. Hell, *Nat. Methods*, 2009, **6**, 24–32.
18 S. T. Hess, T. P. K. Girirajan and M. D. Mason, *Biophys. J.*, 2006, **91**, 4258–4272.

19 M. J. Rust, M. Bates and X. Zhuang, *Nat. Methods*, 2006, **3**, 793–796.
20 E. Betzig, G. H. Patterson, R. Sougrat, O. W. Lindwasser, S. Olenych, J. S. Bonifacino, M. W. Davidson, J. Lippincott-Schwartz and H. F. Hess, *Science*, 2006, **313**, 1642–1645.
21 B. Huang, H. Babcock and X. Zhuang, *Cell*, 2010, **143**, 1047–1058.
22 S. A. Johnson, *WIREs Nanomed. Nanobiotechnol.*, 2015, **7**, 266–281.
23 C. J. Merrifield, M. E. Feldman, L. Wan and W. Almers, *Nat. Cell Biol.*, 2002, **4**, 691–698.
24 S. A. Jones, S. H. Shim, J. He and X. Zhuang, *Nat. Methods*, 2011, **8**, 499–505.
25 J. Wiedenmann and G. U. Nienhaus, *Expert Rev. Proteomics*, 2006, **3**, 361–374.
26 M. J. Rust, M. Lakadamyali, F. Zhang and X. Zhuang, *Nat. Struct. Mol. Biol.*, 2004, **11**, 567–573.
27 O. D. Velev and E. W. Kaler, *Langmuir*, 1999, **15**, 3693–3698.
28 C. Fenzl, T. Hirsch and O. S. Wolfbeis, *Angew. Chem., Int. Ed.*, 2014, **53**, 3318–3335.
29 A. Rogach, A. Susha, F. Caruso, G. Sukhorukov, A. Kornowski, S. Kershaw, H. Möhwald, A. Eychmüller and H. Weller, *Adv. Mater.*, 2000, **12**, 333–337.
30 Y. Y. Diao, X. Y. Liu, G. W. Toh, L. Shi and J. Zi, *Adv. Funct. Mater.*, 2013, **23**, 5373–5380.
31 A. K. Boal, F. Ilhan, J. E. DeRouchey, T. Thurn-Albrecht, T. P. Russell and V. M. Rotello, *Nature*, 2000, **404**, 746–748.
32 J. Rejman, V. Oberle, I. S. Zuhorn and D. Hoekstra, *Biochem. J.*, 2004, **377**, 159–169.
33 Z. Wang, C. Tiruppathi, R. D. Minshall and A. B. Malik, *ACS Nano*, 2009, **3**, 4110–4116.
34 M. Ehrlich, W. Boll, A. van Oijen, R. Hariharan, K. Chandran, M. L. Nibert and T. Kirchhausen, *Cell*, 2004, **118**, 591–605.
35 D. Arcizet, B. Meier, E. Sackmann, J. O. Rädler and D. Heinrich, *Phys. Rev. Lett.*, 2008, **101**, 248103.
36 M. J. Saxton and K. Jacobson, *Annu. Rev. Biophys. Biomol. Struct.*, 1997, **26**, 373–399.
37 T. J. Feder, I. Brust-Mascher, J. P. Slattery, B. Baird and W. W. Webb, *Biophys. J.*, 1996, **70**, 2767–2773.
38 I. F. Sbalzarini and P. Koumoutsakos, *J. Struct. Biol.*, 2005, **151**, 182–195.
39 X. Jiang, S. Weise, M. Hafner, C. Röcker, F. Zhang, W. J. Parak and G. U. Nienhaus, *J. R. Soc., Interface*, 2010, **7**, S5–S13.
40 C. Y. Tay, M. I. Setyawati, J. Xie, W. J. Parak and D. T. Leong, *Adv. Funct. Mater.*, 2014, **24**, 5936–5955.
41 L. Shang, K. Nienhaus and G. U. Nienhaus, *J. Nanobiotechnol.*, 2014, **12**, 5.
42 A. Kusumi, C. Nakada, K. Ritchie, K. Murase, K. Suzuki, H. Murakoshi, R. S. Kasai, J. Kondo and T. Fujiwara, *Annu. Rev. Biophys. Biomol. Struct.*, 2005, **34**, 351–378.
43 Y. Sako and A. Kusumi, *J. Cell Biol.*, 1994, **125**, 1251–1264.